IRIS AperTO

UNIVERSITÀ DEGLI STUDI DI TORINO

AperTO - Archivio Istituzionale Open Access dell'Università di Torino

Kelvin probe characterization of buried graphitic microchannels in single-crystal diamond

This is the author's manuscript

Original Citation:

Availability:

This version is available http://hdl.handle.net/2318/1509414 since 2016-06-28T15:25:46Z

Published version:

DOI:10.1063/1.4905425

Terms of use:

Open Access

Anyone can freely access the full text of works made available as "Open Access". Works made available under a Creative Commons license can be used according to the terms and conditions of said license. Use of all other works requires consent of the right holder (author or publisher) if not exempted from copyright protection by the applicable law.

(Article begins on next page)

04 December 2024

UNIVERSITÀ DEGLI STUDI DI TORINO

This is an author version of the contribution published on:

Questa è la versione dell'autore dell'opera:

"Kelvin probe characterization of buried graphitic microchannels in single-crystal diamond"

E. Bernardi, A. Battiato, P. Olivero, F. Picollo, E. Vittone

Journal of Applied Physics 117, 024103 (2015)

DOI: 10.1063/1.4905425

The definitive version is available at:

La versione definitiva è disponibile alla URL:

http://scitation.aip.org/content/aip/journal/jap/117/2/10.1063/1.4905425

Kelvin probe characterization of buried graphitic microchannels in single-crystal diamond

E. Bernardi[1,2]*, A. Battiato[1,2], P. Olivero[1,2], F. Picollo[2,1], E. Vittone[1,2]

[1] *Physics Department, CNISM and "NIS" Inter-departmental centre, University of Torino, Torino, Italy*

[2] *Istituto Nazionale di Fisica Nucleare (INFN), Sezione di Torino, Torino, Italy*

* corresponding author: ettore.bernardi@unito.it

Abstract

In this work, we present an investigation by Kelvin Probe Microscopy (KPM) of buried graphitic microchannels fabricated in single-crystal diamond by direct MeV ion microbeam writing. Metal deposition of variable-thickness masks was adopted to implant channels with emerging endpoints and high temperature annealing was performed in order to induce the graphitization of the highly-damaged buried region. When an electrical current was flowing through the biased buried channel, the structure was clearly evidenced by KPM maps of the electrical potential of the surface region overlying the channel at increasing distances from the grounded electrode. The KPM profiling shows regions of opposite contrast located at different distances from the endpoints of the channel. This effect is attributed to the different electrical conduction properties of the surface and of the buried graphitic layer. The model adopted to interpret these KPM maps and profiles proved to be suitable for the electronic characterization of buried conductive channels, providing a non-invasive method to measure the local resistivity with a micrometer resolution. The results

24 demonstrate the potential of the technique as a powerful diagnostic tool to monitor the functionality
25 of all-carbon graphite/diamond devices to be fabricated by MeV ion beam lithography.
26

27 ## I. Introduction

28 The existence at ambient conditions of different allotropic forms of carbon with radically different
29 structural and electrical properties (most importantly, diamond and graphite) is an important feature
30 allowing the fabrication of all-carbon devices for various technological applications. In this context,
31 the employment of focused MeV ion beams in diamond is a versatile tool to create different
32 structural forms of carbon by the progressive conversion of the sp^3-bonded diamond lattice to a
33 sp^2-bonded amorphous/graphitic phase[1]. This effect is related to the ion-induced formation of
34 structural defects (vacancies, interstitials and more extended complexes) in the crystal lattice, with a
35 strongly non-uniform depth profile that determines the creation of highly-damaged layers at a depth
36 of the order of micrometer within the crystal bulk, depending on the ion energy (see for example
37 Fig. 1). Ion beam implantation in diamond was extensively applied for the fabrication of a broad
38 range of devices: waveguides[2,3], photonic structures[4,5,6] micromechanical resonators[7,8]. In particular,
39 the possibility of creating graphitic and electrically conductive regions allowed the fabrication of
40 infrared radiation emitters[9], field emitters[10], bolometers[11], biosensors[12] and ionizing radiation
41 detectors[13, 14].
42 The charge conduction mechanisms in amorphized/graphitized diamond have been investigated in
43 previous works[15,16,17]. In the case of buried conducting layers and channels, the analyses were based
44 on current-voltages characterizations carried out by probing 2 or 4 terminals emerging at the surface
45 through conductive columns fabricated by laser induced graphitization[18], high-voltage-induced
46 thermal breakdown[19] or by modulating ion penetration depths by multiple energy ion implantation[20]
47 or variable-thickness metallic masks[21].

48 However, to our best knowledge, because of the inaccessibility of the buried conductive regions, no
49 local microscopic analyses of their electrical properties have been so far performed. They could be
50 effectively explored by scanning probe microscopy techniques such as Electric Force Microscopy
51 (EFM)[22] and Kelvin Probe Microscope (KPM)[23,24], but these techniques are mainly used to
52 investigate the surface electrical properties of semiconductors and insulators, such as the potentials
53 of different terminations of diamond surface[25,26]. It has to be underlined that KPM has been used
54 for the study of the buried interface between diamond and a thin film (25 nm) of polypyrolle[27] and ,
55 recently, for the spectrally and spatially resolved photovoltage measurement of a Schottky junction
56 made of a 4 nm thin tungsten-carbide layer on oxygen-terminated boron-doped diamond [28].On the
57 other hand, they have been rarely used to study deeper buried structures, as in the case of the
58 detection of metal-polymer interfaces buried under a 100 nm polymer thick film[29].
59 In this work we demonstrate the possibility of imaging the electronic properties of deep (1 μm)
60 buried graphitic structures in diamond by scanning probe microscopy. KPM maps and profiles were
61 taken with sub-micrometric spatial resolution in the presence of a steady DC current flowing in the
62 channels, in order to characterize the device in working conditions
63 Results are analysed by modelling both the capacitance couplings and the voltage drops between the
64 buried channels and the conductive surface.

65 II. Experimental

66 A. Ion Beam Fabrication

67 Ion implantation was performed on a synthetic single crystal diamond produced by HPHT (High
68 Pressure High Temperature) process and classified as type Ib on the basis of single substitutional
69 nitrogen ([N] ~ 10 ÷ 100 ppm) content. The crystal was cut along the [100] crystallographic
70 direction and it was polished on the large face that was microfabricated and characterized. The
71 sample was implanted at the AN2000 accelerator of the INFN - Legnaro National Laboratories[30]

72 with a scanning focused 1.2 MeV He^+ ion beam at a fluence of ~10^{17} cm^{-2}. The beam spot size was
73 ~10 µm and the beam current was comprised between 2 nA and 3 nA. Before the implantation
74 process, the diamond surface was covered with a 1 µm thick copper layer in order to reduce the ion
75 penetration depth to the desired value (1 µm). Furthermore, variable thickness masks were
76 employed in order to realize damaged structures with endpoints emerging up to the surface[21].
77 Figure 1 shows the depth profile of the ion-induced structural damage, being parameterized as the
78 volumetric density of induced vacancies, as resulting from SRIM 2013.00 Monte Carlo code[31] in
79 "Detailed calculation with full damage cascades" mode, by setting a displacement energy value of
80 50 eV[32]. As already pointed out in previous works[33], the vacancy-density profile was obtained by
81 modelling the effect of cumulative ion implantation on the number of vacancies with a simple linear
82 approximation, which does not take into account complex processes such as self-annealing, ballistic
83 annealing and defect-defect interaction, therefore such value can only be considered as an effective
84 parameter quantifying the induced damage density. The implantation resulted in the formation of
85 sub-superficial amorphized layers, structured in one longitudinal channel and two transverse
86 channels, located at ~1 µm below the surface.
87 After removal of the copper mask, thermal annealing at 1000 °C for 1 hour was performed to
88 induce the graphitization of the highly-damaged buried region, where the vacancy densities exceeds
89 a threshold value estimated as ~9×10^{22} cm^{-3} in previous works[34,21]. As a result, the buried
90 amorphized regions converted to ~200 nm thick graphitic channels located at the above-mentioned
91 depth (see the highlighted region of the profile in figure 1). Finally, the endpoints were contacted
92 with metal pads: a Cr/Cu deposition was followed by 400 °C heating for 1 hour to create a
93 conductive carbide compound with chromium. In figure 2 an optical micrograph (a) and a 3D model
94 of the final device (b) are shown: two transversal channels emerge at the diamond surface in four
95 locations highlighted by red circles. At each side of the main longitudinal channel, the pair of
96 emerging points is short-circuited through the common surface metal deposition.

97 **B. Current-voltage characteristics**

98 The current-voltage characteristics of the channels were measured at room temperature with a
99 Keithley 2636 electrometer in a standard two-electrode configuration, by using two micro-tip
100 probes in contact with the two Cr/Cu metal electrodes deposited onto the channel endpoints.
101 Surface conductivity was measured using two similar control electrodes not connected to the
102 graphitic channel.

103 **C Atomic force microscopy**

104 A Park Scientific XE-100 AFM equipped with rectangular Au-Cr-coated cantilevers (NSC-14
105 Cr-Au, MikroMash, spring constant of ~5.7 N m^{-1} and resonance frequency between 160 kHz and
106 170 kHz) was used to perform a morphological characterization of the microfabricated sample. The
107 Typical scanning areas were 35×35 μm^2 and the scanning rate was 0.5 Hz. The oscillation
108 frequency of the cantilever was near the resonance on the upper-side. The morphology of the
109 sample was recorded in non-contact, amplitude modulation mode.

110 **D Kelvin Probe Microscopy**

111 In KPM measurements the AC voltage applied to the cantilever tip was set to V_{ac} = 2.5 V and a DC
112 voltage V_{app} = 3.5 V was applied to one of the surface electrodes while the other (left) electrode was
113 grounded in order to have a current flowing through the longitudinal buried channel (figure 2b). The
114 electrostatic forces at frequency v = 17 kHz were minimized by a feed-back loop controlling the DC
115 voltage V_{dc} applied to the tip. Typical scanning areas were 35×5 μm^2 at a scanning rate of 0.2 Hz. In
116 all the experiments, V_{ac} and V_{dc} were applied directly by the control unit of the AFM microscope,
117 whereas a Keithley 614 electrometer was used as external voltage source for V_{app}. The cantilever
118 was oriented parallel to the long axis of the electrodes to minimize artifacts due to the capacitance
119 between the cantilever beam and the electrodes[35].

120

121 ## III. Results and discussion

122 Voltage-current characteristics of the surface and of the buried channels (data not reported here)
123 exhibit a linear ohmic behaviour, in agreement with was reported in Picollo et al.[21]. The electrical
124 resistance of the buried graphitic channel results R_c =3.44 kΩ, a value which is negligible compared
125 to the resistance of the surface (R_s = 493 GΩ), which is attributed to a surface conductive layer
126 induced by the high temperature annealing of the sample[36].
127 The topography profile above the buried channel is reported in figure 2c, which shows a
128 pronounced surface swelling of ~100 nm localized at the implanted area**.** The presence of surface
129 swelling in implanted diamonds is a well know effect[37,38,39] due to the lower density of the graphitic
130 channel with respect to the one of the surrounding diamond crystal.
131 As shown in figures 3a and 3b, KPM maps of dimensions 35×5 μm^2 were acquired across the
132 longitudinal channel at different distances from the left electrode (points "a" and "b" in figure 2a).
133 The KPM maps clearly show a central plateau in correspondence of the buried channel. As
134 expected, the KPM maps are not remarkably influenced by the topography of the surface (i.e.
135 swelling shown in the AFM map in figure 2c) as proven by the inversion of the contrast, when
136 probing regions close to the grounded (figure 3a) or the biased (figure 3b) electrode.
137 To analyse in more detail the behaviour of the contrast in the KPM maps, transversal profiles (i.e.
138 along the y axis) were extracted from KPM maps similar to those shown in figures 3a and 3b and
139 centred in different positions along the channel (coloured dashed segments in figure 2a). Figure 3c
140 shows these profiles relevant to 7 different positions distributed along the x axis from the grounded
141 (left) to the biased (right) electrode. Figure 4 summarizes the different behaviour of the average
142 KPM signals relevant to the surface (i.e. far from the buried channel, ${}^{KPM}V_S$) and to the buried
143 channel (${}^{KPM}V_C$) as a function of the x position. In order to remove the effects of the contact
144 potential and of the intrinsic surface potential[40], all the KPM signals have been subtracted to the

145 reference signal measured with both grounded electrodes. Moreover, this procedure minimizes any
146 possible influence of surface contaminations on the KPM measurements[41,42].
147 From the inspection of figure 4, the following considerations can be made:
148 i) the KPM signals from both the regions directly above and aside the buried channel increase
149 when moving from the grounded electrode to the electrode biased at V_{app} = +3.5 V;
150 ii) near the grounded left electrode, the KPM signal on the region directly above the buried channel
151 is larger than the baseline, while the opposite happens near the right electrode; in between, a
152 cross-over between the two profiles is observed.
153 To understand this behaviour we have to consider that the KPM signal corresponds to the V_{dc} that
154 minimize local electrostatic force F_{ω} induced by several conductive elements present in the
155 system[43,44]. In this case the local force sensed by the "tip + cantilever" system at a distance x from
156 the left electrode $F(x)$ is the sum of the contributions relevant to all the conductive elements,
157 namely the surface conductive layer (F_0), the longitudinal buried channel (F_1), the left and right
158 electrodes (F_2, F_3) and the left and right transversal channel (F_4, F_5). The i-th force $F_i(x)$ at point x
159 depends on the potential ($V_i(x)$) generated by the i-th conductive element and on the capacitive
160 coupling $K_i(x)$ between the "tip + cantilever" system and the i-th conductive element, i.e.:

$$(\ ) \quad \sum \quad (\ ) \quad \sum \quad (\ )[\quad (\ )] \quad (\quad)$$

161 (1)

162 The KPM signal (^{KPM}V) is then given by:

$$\frac{\sum \ (\ ) \ (\ )}{\sum}$$

163 (2)

164 Equation (2) implies that the KPM signal is the weighted average of the potentials associated to the
165 different conductive elements, the weighting factors being the capacitive coupling of the conductive
166 elements with the tip. We note that these terms decrease with the increasing of the distance from the
167 conductive element to the "tip + cantilever" system[43], hence, far from the electrodes, the dominant
168 terms in the sums of equation 4 are related to the surface (K_0) and to the buried channel (K_1).

169 Regarding the contribution in equation (2) relevant to the surface ($V_0(x)$) it can expressed as the
170 interelectrode (w = 220 μm) potential drop:

171 − (3)

172 $V_0(x)$ is indicated by the dashed line in figure 4.
173 Furthermore, we can safely assume that far away from the buried channel, the term related to the
174 longitudinal buried channel in equation (2) (i = 1) can be neglected, and, by plotting V_0 as function
175 of the experimental KPM signal relevant to the surface (${}^{KPM}V_S$), it is apparent that the contribution
176 of all the other terms provide a linear relationship (figure 5a), i.e. . The
177 coefficients $a = (0.65 \pm 0.06)$ V and $b = (0.62 \pm 0.03)$, extracted from the linear fit of the
178 experimental data, can be considered as defining the transfer function, which correlate the KPM
179 signal to the real potential at point x. In particular, at point x located onto the buried channel, the
180 KPM signal , filtered from the contribution of the left and right electrodes (F_2, F_3) and
181 transversal channel (F_4, F_5) can be evaluated through the expression: (4)

182

183 as shown in figure 5b.
184 Actually, the macroscopic electrostatic tip-sample interaction can be calculated from the potential
185 energy: (5)

186 − −

187 stored in the two capacitors in series formed between the tip/surface and surface/channel. The free
188 energy ( ) of the system can then be calculated by the sum of the two capacitor contributions and
189 by the work done by the sources[45]:

190 ( ) (6)

191

192 By virtue of the high resistance of the surface, in equation (5) the work done by the voltage source
193 was consider acting only in maintaining fixed V_I, whereas V_0 is let free to change according to the
194 potential related to the charge induced by V_I onto the surface, minimizing the electrostatic energy
195 along the z direction, it is found that $^{KPM}V_C$ is equal to V_I.
196 Such an interpretation is further corroborated by the potential drop calculated from elementary
197 circuital analysis of the five resistances drawn in the inset in figure 5b, i.e. four parallel transversal
198 resistances of lengths d_i (i = 1, 4) and one longitudinal resistance of length d_L+d_R+w. Assuming a
199 constant resistivity of the graphitic channel and a constant section of the buried channel, the
200 potential $V_I(x)$ is given by:

$$(\,) \qquad (\quad) \, (\quad) \qquad (7)$$

201
$$\frac{(\quad) + (\quad)}{— — \quad — —}$$

202 it is worth noting that, apart from a slight shift, V_I is close to the experimental data corrected by the
203 linear transfer function (, see figure 5b.
204 Finally, it is worth remarking that the abovementioned analysis provides a method to locally
205 evaluate the channel resistivity. In fact, the slope of the experimental potential drop along the
206 channel ( ) is connected to the graphitic channel resistivity ρ by the
207 following relationship: $(\quad)$ (8)

208 $- \quad \overline{\qquad}$

209 where A is the channel section (200 nm × 12 μm), I is the current (1.04 mA) flowing through the
210 graphitic channel. Such a value is in good agreement with the typical resistivity values measured for
211 standard polycrystalline graphite (ρ = 3.5 mΩ cm)[21,46].
212 It is worth remarking that the linear behaviour of the data point implies the
213 homogeneity of the resistance along the main axes of the channel.

214 Lastly, it has to be underlined that the asymmetries in the device geometry do not significantly
215 affect our key findings. Indeed, the lack of symmetry in the positioning of the metal electrodes
216 results only in a shift of the cross-over between the two profiles of figure 4 from the mid-point
217 between the two electrodes to a position slightly closer to the left electrode. Furthermore, the
218 definition of two transversal channels and their slight asymmetry with respect to the axis of the
219 longitudinal channel result substantially in the addition of two resistors in parallel at each side of the
220 buried channel equivalent circuit depicted in the inset of figure 5b.

221 IV. Conclusions

222 Sub-superficial graphitic microchannels fabricated in single-crystal diamond with a deep ion beam
223 fabrication technique were characterized by mapping the electrostatic properties of the sample by
224 probing in non-contact mode the electrostatic tip-sample force. KPM was proven to be suitable to
225 map graphitic channels buried at a depth of 1 μm. KPM maps represent the actual electrical images
226 of the graphitic channels, since they are practically insensitive from the surface morphology. The
227 model adopted to interpret these maps provides a non-invasive method to measure the local
228 resistivity of buried conductive channels. For the case of study, the constant potential drop across
229 the buried channel evidences a uniform distribution of resistivity, whose value is in agreement with
230 that of polycrystalline graphite.
231 These results have significant implications for the fabrication of all-carbon graphite/diamond
232 devices; in facts, they have demonstrated the potential of the technique to non-invasively map with
233 a micrometer resolution and in working conditions, the electrical properties of more complex buried
234 graphitic patterns, which can be directly written by MeV ion beam lithography in diamond[47].
235
236

237 ## Acknowledgments

238 This research activity was supported by the following projects: FIRB project D11J11000450001
239 funded by MIUR; “A.Di.NTech.” project D15E13000130003 and “2011-Linea 1A” project
240 ORTO11RRT5 funded by the University of Torino-Compagnia di San Paolo; “DiNaMo” (young
241 researcher grant, project n° 15766) by National Institute of Nuclear Physics.

242

243 # Figures Captions

244 **Fig. 1** Vacancy density profile induced by 1.2 MeV He^+ ions at a fluence of 1×10^{17} cm^{-2} in diamond
245 covered by a 1-µm-thick copper layer as calculated by SRIM2013.00 Monte Carlo simulations. The
246 dashed region in the graph represents the highly damaged buried region where the thermal
247 annealing induces the graphitization, due to the vacancy densities exceeding a critical threshold.
248

249 **Fig. 2 (a)** Optical micrograph of the buried channels, which lie at ~1 µm below the sample surface.
250 The emerging end-points are highlighted by red circles. All channels are 12 µm wide and the
251 inter-electrode distance is 220 µm. White letters indicates the locations of the KPM maps in figures
252 3 (a,b): dashed lines indicates the locations of the KPM profiles shown in figure 3(c). **(b)**
253 Schematics (not to scale) of the sample and of the KPM experimental setup. Both DC (V_{dc}) and AC
254 (V_{ac}) voltages are applied to the conductive AFM microtip. A second independent DC voltage (V_{app})
255 is applied across the buried graphitic channel. **(c)** Topography profile acquired across the buried
256 channel. The horizontal axis is orthogonal to the graphitic channel.
257

258 **Fig. 3** KPM maps collected from surface regions above the buried channel lying closer to the left
259 (**a**) and the right (**b**) electrode (regions "a" and "b" in figure 2 (a)). The left electrode is grounded;
260 the right electrode is biased at $V_{app} = +3.5$ V. Maps were acquired with the fast scanning direction
261 orthogonal to the channel axis. **(c)** KPM profiles collected across the buried channel at different
262 distances, indicated by dashed lines in figure 2 (a), from the left electrode.
263

264 **Fig. 4** Plots of the KPM signal as a function of the distance from the left electrode, both for regions
265 directly above (black square dots) and away (red circular dots) from the buried channel. The black
266 dashed line represents $V_0(x)$ given by eq. (2).
267

268 **Fig. 5 (a)** Predicted potential at the surface V_0, defined by eq. 3, as function of experimental
269 potential KPM signal ^{KPM}V. The dot-dashed line is the best-fit line. (**b**) Experimental ($^{KPM}V_c(x)$, red
270 filled circles) and corrected by the linear transfer function in eq. (4) ($^{KPM}V_c^{corr}(x)$, red hollow
271 circles) potential drop from KPM signal. The line is the predicted potential drop (eq. 7) derived
272 from the equivalent circuit schematically drawn in the inset.

273

274

275 **Fig. 1**

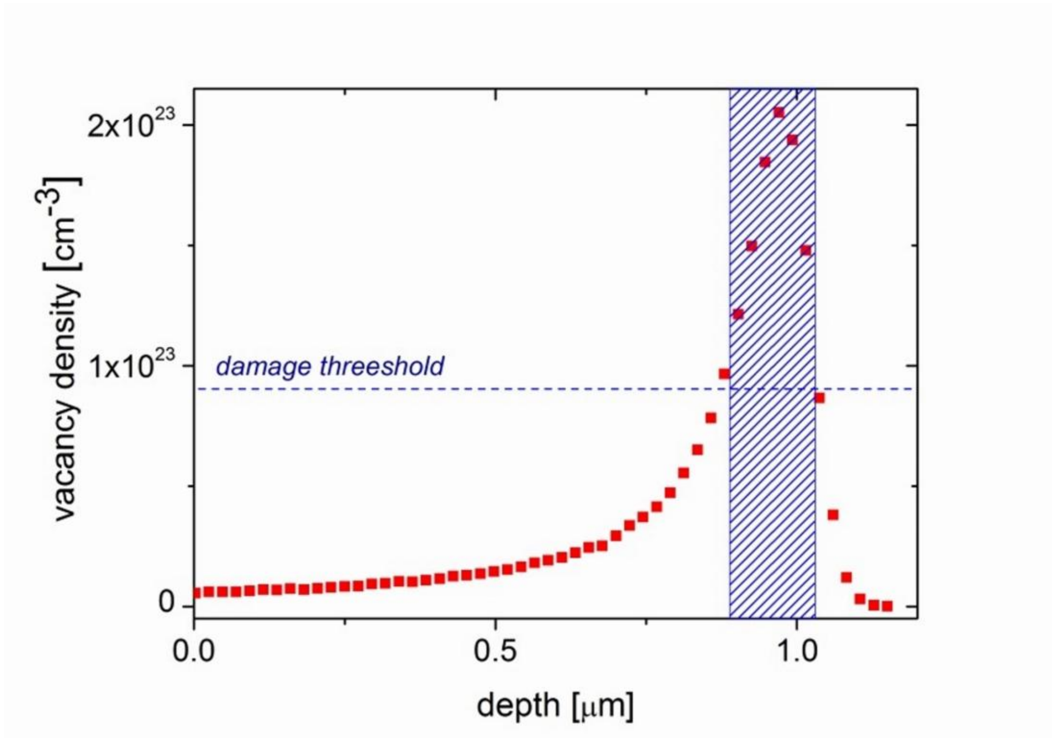

276

277

278 **Fig.2**

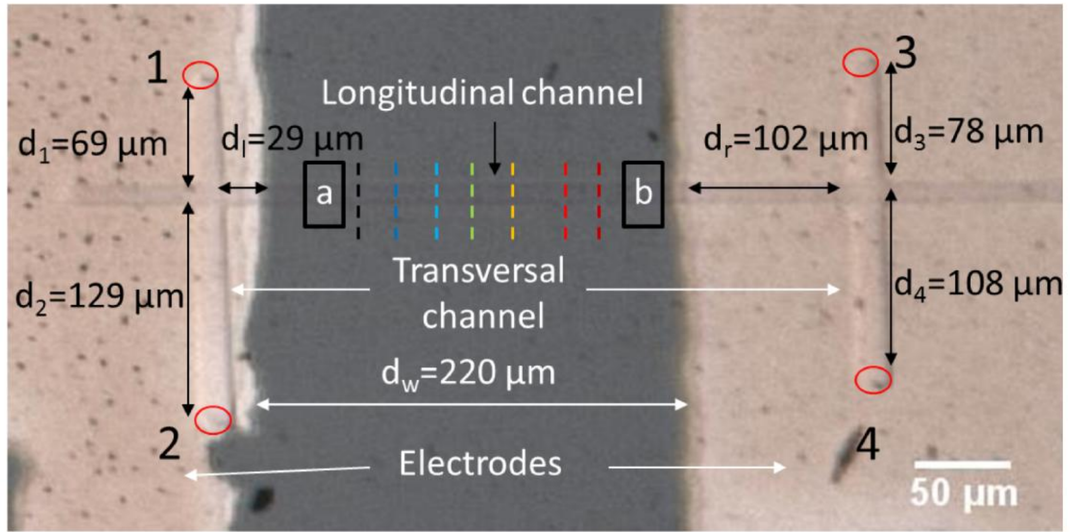

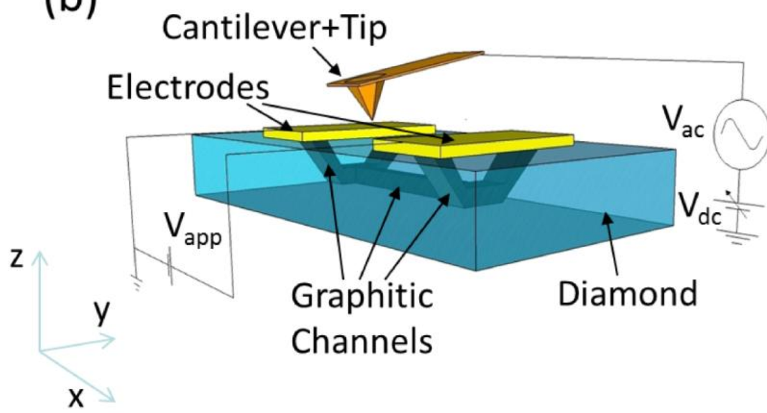

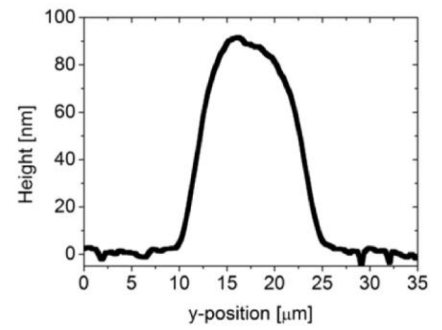

279

280

281

282 **Fig. 3**

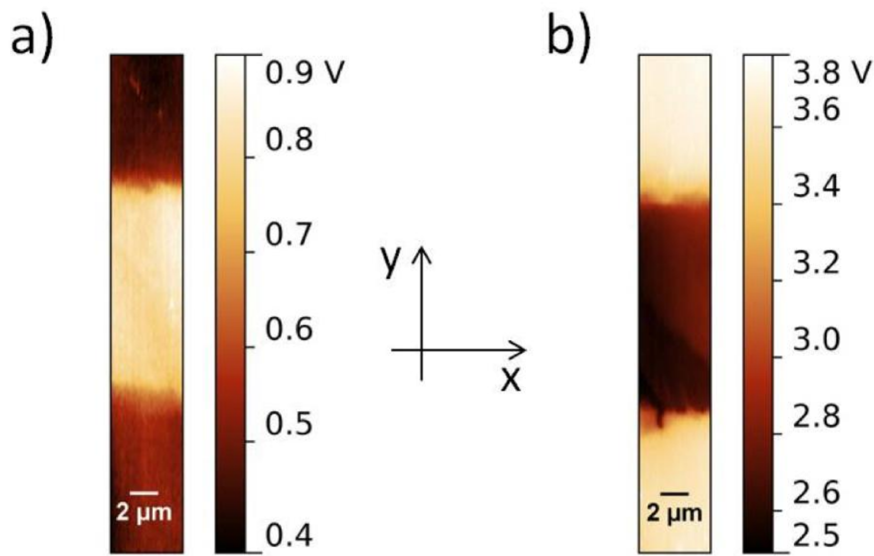

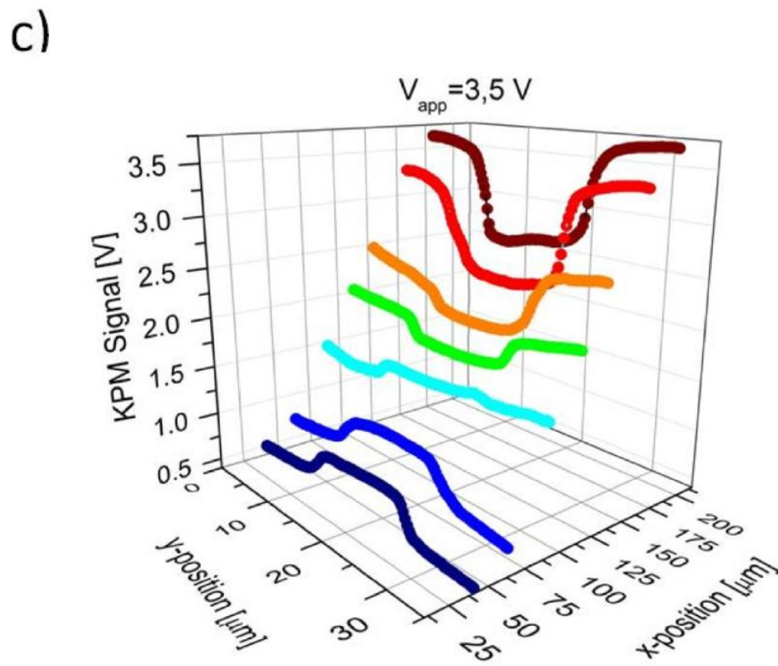

283
284

285

286 **Fig. 4**
287

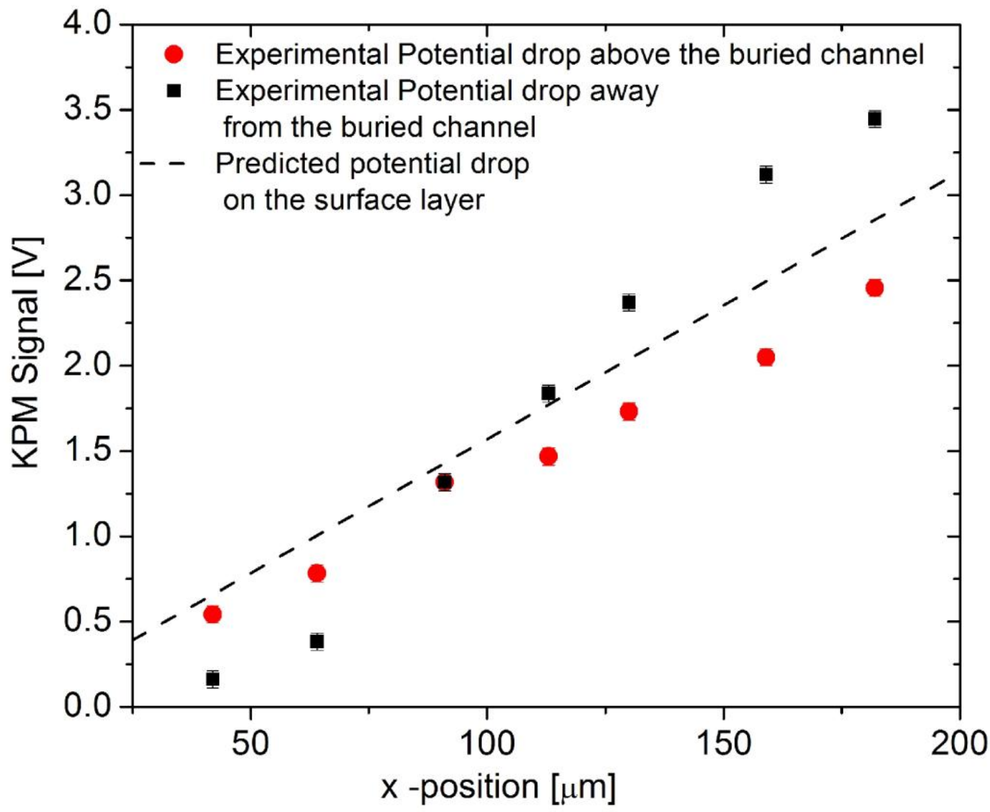

288
289

290

291

292 **Fig. 5**

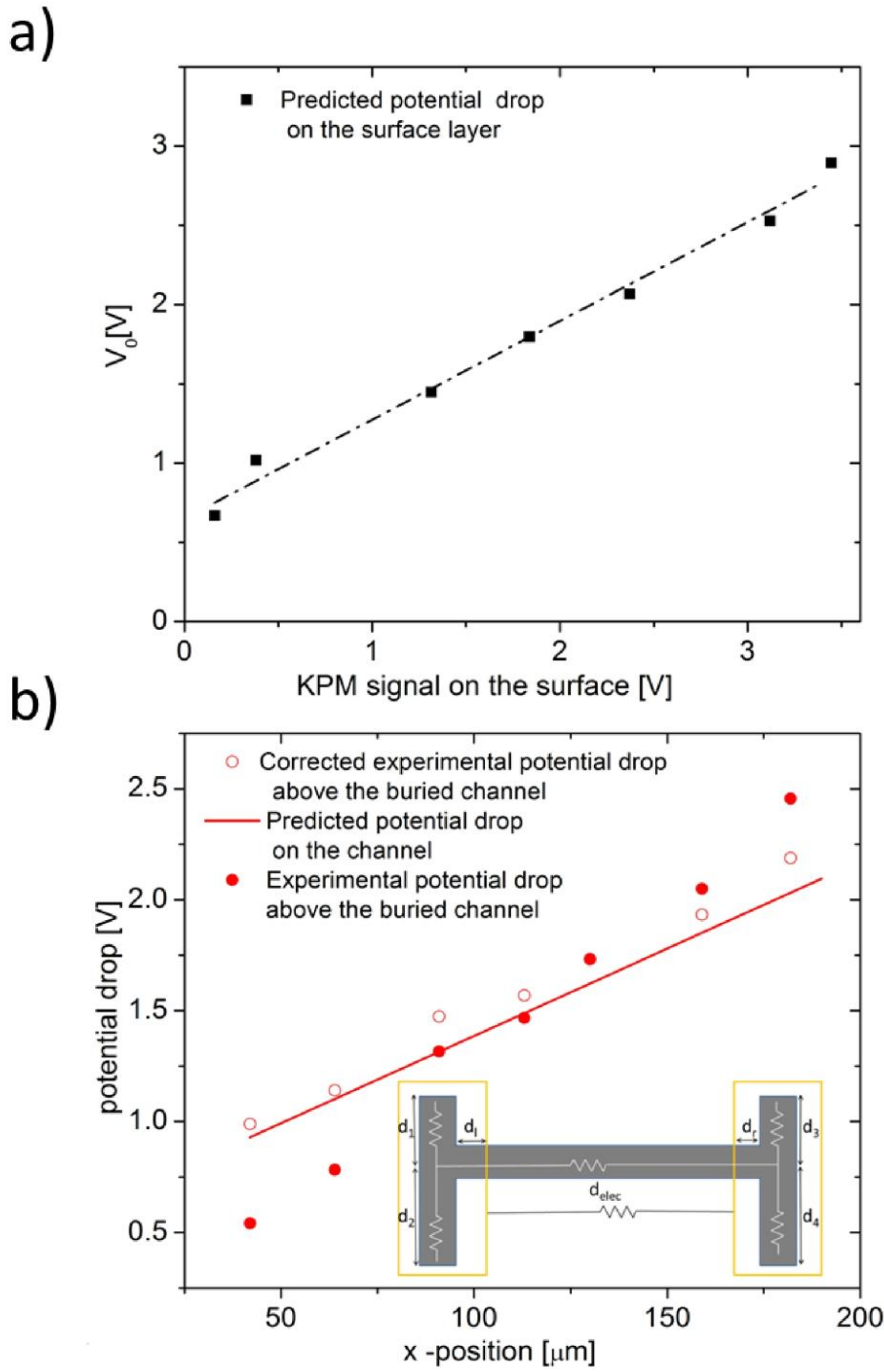

293

294

295

296

297 References

298 [1]S. Prawer, D. N. Jamieson, R. Kalish, Physical Review Letters **69** , 2991 (1992)

299 [2]P. Olivero, S. Rubanov, P. Reichart, B. C. Gibson, S. T. Huntington, J. Rabeau, A. D. Greentree, J.
300 Salzman, D. Moore, D. N. Jamieson, S. Prawer, Advanced Materials **17**, 2427 (2005)

301 [3]M. P. Hiscocks, K. Ganesan, B. C. Gibson, S. T. Huntington, F. Ladouceur, S. Prawer, Optics
302 Express **16**, 19512 (2008)

303 [4]I. Bayn, B. Meyler, A. Lahav, J. Salzman, R. Kalish, B. A. Fairchild, S. Prawer, M. Barth, O.
304 Benson, T. Wolf, P. Siyushev, F. Jelezko, J. Wrachtrup, Diamond and Related Materials **20**, 937
305 (2011)

306 [5] J. C. Lee, I. Aharonovich, A. P. Magyar, F. Rol, E. L. Hu, Optics Express **20**, 8891 (2012)

307 [6]B. R. Patton, P. R. Dolan, F. Grazioso, M. B. Wincott, J. M. Smith, M. L. Markham, D. J.
308 Twitchen, Y. Zhang, E. Gu, M. D. Dawson, B. A. Fairchild, A. D. Greentree, S. Prawer, Diamond
309 and Related Materials **21**, 16 (2012)

310 [7]M. Liao, S. Hishita, E. Watanabe, S. Koizumi, Y. Koide, Advanced Materials **22**, 5393 (2010)

311 [8]M. K. Zalalutdinov, M. P. Ray, D. M. Photiadis, J. T. Robinson, J. W. Baldwin, J. E. Butler,
312 T. I. Feygelson, B. B. Pate, B. H. Houston, Nano Letters **11**, 4304 (2011)

313 [9]S. Prawer, A. D. Devir, L. S. Balfour, R. Kalish, Applied Optics **34**, 636 (1995)

314 [10]A. V. Karabutov, V. G. Ralchenko, I. I. Vlasov, R. A. Khmelnitsky, M. A. Negodaev, V. P.
315 Varnin, I. G. Teremetskaya, Diamond and Related Materials **10**, 2178 (2001)

316 [11]A. I. Sharkov, T. I. Galkina, A. Y. Klokov, R. A. Khmelnitskii, V. A. Dravin, A. A. Gippius,
317 Vacuum **68**, 263 (2003)

318 [12]F. Picollo, S. Gosso, E.Vittone, A. Pasquarelli, E. Carbone, P. Olivero, V. Carabelli, Adv. Mater.
319 **25**, 4696 (2013)

320 [13]P. J. Sellin, A. Galbiati, Applied Physics Letters **87**, 093502 (2005)

321 [14]J. Forneris, V. Grilj, M. Jakšić, A. Lo Giudice, P. Olivero, F. Picollo, N. Skukan, C. Verona, G.
322 Verona-Rinati, E. Vittone, Nucl. Instr. Meth. in Phys. Res. B, **306**, 181-185 (2013)

323 [15] J. F. Prins, Physical Review B **31**, 2472-2478 (1985).

324 [16]R. Kalish, A. Reznik, K. W. Nugent, S. Prawer, Nucl. Instr. Meth. in Phys. Res. B **148**, 626
325 (1999)

326 [17]E. Baskin, A. Reznik, D. Saada, J. Adler, R. Kalish, Physical Review B **64**, 224110 (2001)

327 [18] R . Walker, S. Prawer, D.N. Jamieson and K.W. Nugent, Appl. Phys. Lett. **71**, 1492 (1997)

328 [19]A.A. Gippius, R.A. Khmelnitskiy, V.A. Dravin and S.D. Tkachenko, Diamond Relat. Mater. **8**,
329 1631 (1999)

330 [20] T .I. Galkina, A.Y. Klokov, A.I. Sharkov, R.A. Khmelnitski, A.A. Gippius, V.A. Dravin, V.G.
331 Ral'chenko and A.V. Savel'ev, Phys. Solid State **49** 654 (2007)

332 [21]F. Picollo , D. Gatto Monticone , P. Olivero , B. A. Fairchild , S. Rubanov , S. Prawer , E. Vittone,
333 New Journal of Physics **14**, 053011 (2012)

334 [22]P. Girard, Nanotechnology **12**, 485–490 (2001)

335 [23]Y. Martin,D.W. Abraham and H.K. Wickramasinghe, Appl. Whys. Len., **52,** 1103 (1988).

336 [24]W. Melitz, J.Shen, A. C. Kummela, S. Lee, Surface Science Reports **66**, 1 (2011)

337 [25]B. Rezek, C.E. Nebel, Diamond and Related Materials **14,** 466 (2005)

338 [26]M. Tachiki,. Y. Sumikawa, M. Shigeno., H. Kanazawa, T. Banno, K. Soup Song, H. Umezawa, H.
339 Kawarada, Surface Science **581,** 207 (2005)

340 [27]B. Rezek , J. Čermák, A. Kromka, M. Ledinský, J. Kočka, Diamond Relat. Mater. **18**, 249 (2009)

341 [28]J. Čermák, Y. Koide, D. Takeuchi and B. Rezek, Journal of Applied Physics **115**, 053105 (2014)

342 [29] M.M. Marzec, K. Awsiuk, A. Bernasik, J. Rysz , J. Haberko ,W. Łużny , A. Budkowski, Thin
343 Solid Films **531,** 271(2013)

344 [30] D. Bollini, F. Cervellera, G.P. Egeni, P. Mazzoldi, G. Moschini, P. Rossi, V. Rudello, Nucl. Instr.
345 and Meth. A **328**, 173 (1993)

346 [31] [http://www.srim.org/]

347 [32]W. Wu, S. Fahy, Physical Review B **49**, 3030 (1994)

348 [33] F. Bosia, N. Argiolas, M. Bazzan B. Fairchild, D. Greentree, D. W. M. Lau, P. Olivero, F.
349 Picollo, S. Rubanov, S. Prawer, J. Phys. Condens. Matter 25, 385403 (2013)
350 [34]P. Olivero, S. Rubanov, P. Reichart, B. C. Gibson, S. T. Huntington, J. R. Rabeau, A. D.
351 Greentree, J. Salzman, D. Moore, D. N. Jamieson, S. Prawer, Diamond and Related Materials **15**,
352 1614-1621 (2006)
353 [35.] K. Puntambekar, P. Pesavento, and C. Frisbie, Applied. Physics. Letters **83,** 5539
354 [36] Yu. V. Butenko, V. L. Kuznetsov, A. L. Chuvilin, V. N. Kolomiichuk, S. V. Stankus, R. A.
355 Khairulin, and B. Segall, Journal of Applied Physics **88**, 4380 (2000)
356 [37]J. F. Prins, T. E. Derry, J. P. F. Sellschop, Physical Review B **34**, 8870-8874 (1986)
357 [38]F. Bosia, S. Calusi, L. Giuntini, S. Lagomarsino, A. Lo Giudice, M. Massi, P. Olivero, F. Picollo,
358 S. Sciortino, A. Sordini, M Vannoni, E Vittone. Nucl. Instr. Meth. B **268,** 2991, (2010)
359 [39] M. Piccardo, F. Bosia, P. Olivero, N. Pugno, Diamond & Related Materials **48**, 73 (2014)
360 [40] D. J. Bayerl and X. Wang Adv. Funct. Mater. **22**, 652 (2012)
361 [41]H. Bluhm, T. Inoue, M. Salmeron, Surface Science **462**, 602 (2000)
362 [42] W.W.R. Araoujo, M.C. Salvadori, F.S. Teixeira, M. Cattani, I.G. Brown, Microscopy Research
363 And Technique **75**, 977 (2012)
364 [43]H.O. Jacobs, P. Leuchtmann, O.J. Homan and A. Stemmer, Journal of Applied Physics **84**, 1168
365 (1998)
366 [44]D. Brunel, D. Deresmes, and T.Mélin, Applied Physics Letters **94**, 223508 (2009)
367 [45] A. Sadeghi, A. Baratoff, S. Alizera Ghasemi, S. Goedecker, T. Glatzel, S Kawai, and E. Meyer
368 Physical Review B **86**, 075407 (2012)
369 [46] J.D. Cutnell and K.W Johnson, Resistivity of Various Materials in Physics (New York: Wiley)
370 2004
371 [47] F. Picollo, A. Battiato, E. Bernardi, L. Boarino, E. Enrico, J. Forneris, D. Gatto Monticone, P.
372 Olivero, arXiv:1412.2212
373